Mechanochemistry in [6]Cycloparaphenylene: A Combined Raman Spectroscopy and Density Functional Theory Study

Mechanochemistry in [6]cycloparaphenylene. A combined Raman spectroscopy and density functional theory study

Lili Qiu[1,a], Miriam Peña-Alvarez[2-3,a], Valentín G. Baonza[2], Mercedes Taravillo[2], Juan Casado*[4], and Miklos Kertesz*[1]

[1]Department of Chemistry and Institute of Soft Matter, Georgetown University, 37th and O Streets, NW, Washington, D.C., 20057-1227, USA.

[2]MALTA-Consolider Team, Department of Physical Chemistry I, Chemistry Faculty, University Complutense of Madrid, 28040 Madrid, Spain.

[3]Centre for Science at Extreme Conditions, The University of Edinburgh, King's Buildings, Edinburgh, UK.

[4]Department of Physical Chemistry, University of Málaga, CEI Andalucía Tech, Campus de Teatinos s/n, 29071-Málaga, Spain.

[a]These authors contributed equally to this work.

Abstract

Raman spectroscopy under high pressures up to 10 GPa and density functional computations up to 30 GPa are combined to obtain insights into the behavior of a prototypical nanohoop conjugated molecule, [6]cycloparaphenylene, [6]CPP. Upon increasing pressure the nanohoop undergoes deformations, first reversible ovalization and then at even higher pressures aggregates are formed. This irreversible aggregation is due to the formation new intermolecular σ-bonds. Frequencies and derivatives of the Raman frequency shifts as a function of pressure are well reproduced by the computations. The frequency behavior is tied to changes in aromatic/quinonoid characters of the nanohoop. The modeling at moderate high pressures reveals the deformation of the [6]CPP molecules into oval-like and peanut-like shapes. Surprisingly the pressure derivatives of the observed Raman mode shifts undergo a sudden change around a pressure value that is common to all Raman modes, indicating an underlying geometrical change extended over the whole molecule that is interpreted by the computational modeling. Simulations predict that under even larger deformations caused by higher pressures, oligomerization chemical reactions would be triggered. Our simulations demonstrate that these transformations would occur regardless of the solvent, however pressures at which they happen are influenced by solvent molecules encapsulated in the interior of the [6]CPP.

I. INTRODUCTION

Recently significant progress has been achieved in the computational modeling of organic materials under high pressures yielding important new theoretical insights.[1,2,3] Mechanochemistry, as this general area of chemistry is referred to, deals with chemical effects of external pressures and forces on molecules and aggregates. This often yields unexpected changes of solid-state and molecular properties and leads to surprising reactivities.[4, 5, 6, 7] A significant bottleneck of the progress of mechanochemistry is the absence of analytical/structural tools at this scale of pressures to build reliable structure-reactivity connections. Quantum chemical modelling can follow and reproduce the available experimental data

bringing us the possibility to establish an account of the mechanochemical event in terms of changes in molecular structures, creation of new reactive intermediates and products.

Molecules consisting of π-conjugated carbon systems with curved surfaces, such as carbon nanotubes, fullerenes, corannulene and sumanene, are fascinating owing to their unique structures, varying degrees of aromaticity and promising applications in material science. The shortest segment of an armchair single wall carbon nanotube[8] can be viewed as a para carbon connected cyclic oligophenylene, or cycloparaphenylene (CPP). An [n]CPP molecule consists of n para-linked phenyl units. They have gained significant attention recently.[9,10,11,12,13,14] Systematic studies of [n]CPPs focused on their size-dependent properties such as HOMO-LUMO energy gaps,[15] Raman spectroscopy,[16] photophysical properties[17,18,19] and redox potentials,[20] and size-complementary host-guest chemistry.[21,22,23] [n]CPPs with their curved conjugated surfaces show great potential for bottom-up synthesis of nanobelts[24] and novel donor-acceptor nanohoop materials.[25] The crystal structures of [n]CPPs are also well established showing that most of [n]CPPs (n=5,7-16 and 18) are herringbone-packed in the solid state except for [6]CPP, which displays a hexagonally-packed tubular arrangement where the CPP units are assembled into columns forming channels. Therefore, [6]CPP crystals, with its hexagonally packed tubular channels, naturally provide extended cavities for solvents or other guest molecules.

Pressure is a powerful tool to modify the structure and properties of the [n]CPPs[26] at constant composition. Furthermore, as [n]CPPs might represent the precursors for a bottom-up synthesis of carbon nanotubes, therefore a detailed knowledge of their reactive characters without introducing extra reagents must be explored and this is uniquely provided by high pressure chemistry. To observe such structural transformations and intermolecular effects, Raman spectroscopy is a valuable nondestructive tool helping to characterize such changes in backbone structure, electron delocalization, molecular conformations and polymorphism under the action of external pressures. High pressure treatment of organic conjugated molecules often leads to intermolecular bond formation accompanied by a loss or partial loss of conjugation.[27] A prominent recent example is provided by the complex phase space of one of the smaller molecules, benzene, which undergoes intermolecular bond formation at about 20 GPa to develop a surprising polymeric phase.[28, 29, 30] Poly-p-phenylene, however, seemingly resists bond formation up to 20 GPa as indicted by the reversibility of the Raman spectra.[31] Three oligo(para-phenylene) materials show systematic changes of the powder X-ray diffraction (PXRD) and Raman spectra up to 6 GPa indicating planarization due to the reduction of interring torsions but without the formation of intermolecular bonds.[32] Based on early experiments, Nicol and Yin went so far as to claim that "…unsaturated C-C bonds will not survive pressures much higher than 10 GPa." Furthermore, detailed X-ray data indicate that the molecular phases of layered "herringbone" structures, such as present in polyacenes[33] and poly-p-phenylenes,[34] remain without loss of conjugation and without formation of intermolecular CC bonds for pressures at least up to limits of these experiments of 9 GPa and 6 GPa, respectively. However, for the fluorene molecule($C_{13}H_{10}$) at about 3.6 GPa the herringbone structure changes towards π-stacking, yet no intermolecular bond formation was observed up to 14 GPa by using PXRD.[35]

In this work we expand this structure-spectroscopy connection by incorporating theoretical modeling and experimental Raman spectra, in the description of the high pressure behavior of a deformable conjugated molecule, [6]cycloparaphenylene, [6]CPP, see Scheme 1 for the chemical structure. Thanks to the correlation between our experimental Raman data and quantum chemical

simulation at high pressure for [6]CPP we are able to interpret the observed pressure dependent vibrational data in terms of reversible molecular deformations and then irreversible aggregation due to the formation of new σ-bonds at the highest pressures in the experimental pressure range studied, up to 7.2 GPa. In addition to Raman spectroscopy experiments, we present computational modeling to monitor the structural responses with respect to varying pressures by geometry optimization. Through analyzing Raman vibrational shifts as a function of pressure, both experimentally and theoretically, we are able to provide information on the anharmonicity of the solid-state deformation produced with pressure by evaluating the mode Grüneisen parameters.[36] The modeling poses a new question regarding the elastic or plastic pressure-induced deformation of the nanohoop: is the structural collapse upon pressure reversible? What are the limits of the elastic deformation? In this sense, it is known that unfilled carbon nanotubes under high pressures attain highly deformed peanut shapes.[37,38] Do [6]CPP molecules also undergo such internal volume collapse at high pressures? What is the effect of the encapsulated solvent molecules and how do pressure and solvent inclusion affect the Raman spectra? One of the goals of the presented modeling is to find guidance for the interpretation of the observed Raman shifts and then obtain answers these essential questions.

II. METHODOLOGY

II.1 The polymorphism approach: polymorphism is an important factor to be considered in organic solid state chemistry in general, and for [n]CPPs in particular, because it can influence the properties dramatically. Unlike the herringbone packing pattern of all other [n]CPP crystal structures, [6]CPP follows a unique molecular arrangement[10], which involves the linear alignment of molecules forming nanotube-like open channels, whose structures are illustrated in Figure 1a. This polymorph[10] has been recently named the tubular[39] or T-polymorph by Fukushima et al. who found a new polymorph of [6]CPP with a herringbone-packed structure (termed the H-polymorph) by recrystallization of the T-polymorph.[39] Unfortunately, this thermodynamically stable herringbone-packed polymorph has no single crystal XRD structure, however, powder XRD data were used in the reported structure of the new H-polymorph.[39] For consistency, our theoretical models include both the H- and T-polymorphs with and without solvents under varying pressure.

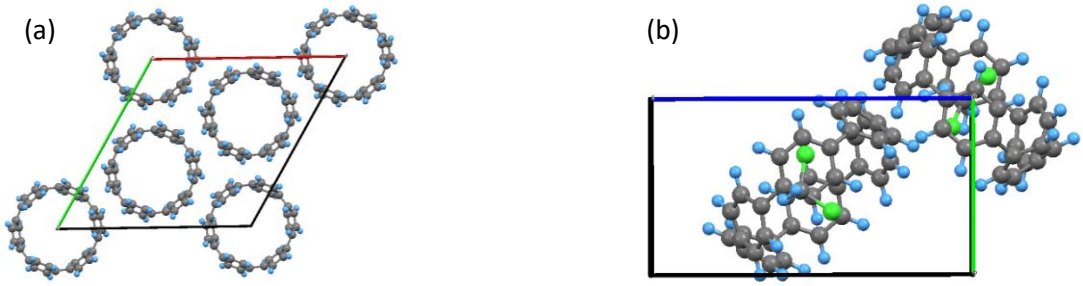

Figure 1. (a) T-polymorph of [6]CPP crystal from single X-ray diffraction (Z=3, top view through c axis, ref 10, the unknown solvent is not shown); (b) H-polymorph solvent-included [6]CPP crystal[39] (Z=2, side view through the a axis). Solvents are dichloromethane molecules.[39] Carbons are grey, hydrogens are blue and chlorines are green.

II.2 Structural parameter approach: we used three pressure-dependent structural parameters to describe the deformation as a function of pressure as follows.

(i) Bond Length Alternation (BLA), computed by eq. (1) and illustrated in Figure 2a, is defined as the average of the distance differences between adjacent bonds. The BLA is a widely used index to indicate the aromatic vs. quinonoid characteristics of conjugated chains and rings, such as poly-p-phenylene[40] or the [n]CPPs,[16] and its importance for Raman intensities has been recognized earlier.[41] BLA>0 indicates an aromatic structure, BLA<0 values correspond to a quinonoid structure. Since the symmetry is reduced with increasing pressures, an average over all six rings must be taken to obtain a reasonable characteristic BLA value for the molecule as a function of pressure.

$$BLA = \text{Average}(r + r_2 - r_1 - r'_1) \qquad (1)$$

(ii) The torsional angles between adjacent phenyl rings (θ in Fig. 2a) also characterize the degree of conjugation and quinonoidization. Given the symmetry breaking at higher pressures of the [6]CPPs, we computed the average torsions between adjacent phenyls as a function of pressure.

(iii) The development of an oval shape under pressure is approximately characterized by the flattening factor f(P), computed by eq. (2), which describes the deviation of the shape of the nanohoop starting from the initial (P=0.1 MPa) cylindrical shape to an overall approximate ellipsoid or even a peanut shape shown in Figures 2b and S1 at high pressure:

$$f(P) = 1 - b(P)/a(P), \qquad (2)$$

where *a* and *b* are the major and minor axis. We obtained *a* and *b* by approximating them by the longest and shortest carbon-carbon distances across the nanohoop at a given pressure.

Figure 2. Geometric parameters characterizing deformed [6]CPPs: (a) CC bond distances (r, r_1, r_1' and r_2) used in the BLA formula in eq. (1) and torsional angle (θ) between two neighboring benzene units. (b) Major (*a*) and minor (*b*) axis of [6]CPP. Carbons are grey, hydrogens are blue.

II.3 Experimental section: [6] CPP was provided by Jasti et al. and synthesized through Suzuki-Miyaural cross-coupling/macrocyclization to macrocycles and their consecutive reduction routes.[10] Different high pressure dependent Raman measurements were carried out. Two spectrometers were used, a Bruker Senterra with a 785 nm excitation wavelength and, ISA HR460 monochromator with a 532.0 nm excitation wavelength. This Raman spectrometer had a spectral resolution of 3 cm^{-1}. The ISA HR460 monochromator had a spectral resolution of about 2−3 cm^{-1}. Calibration was checked using a standard neon lamp. A Spectra-Physics solid state laser, operating at 532.0 nm was used as the excitation source. Both Raman setups had a typical sampling area of about 1−2 μm in diameter. High-pressure experiments were conducted in a sapphire anvil cell (SAC)[42] with a diameter culet of 380 μm and a partially drilled gold gasket. No pressure-transmitting medium was used in order to exclude further species that might be encapsulated or intercalated in the [6]CPP crystals. Five experimental runs were conducted by using new starting samples to reach high pressures ranging between 4 and 10 GPa. Diamond chips were placed in the sample chamber as the pressure calibrant.[42] The frequency region associated with the calibrant bands

(1330 cm^{-1}) was indicated in the experimental spectra with a gray background. Second derivative analysis of the spectra combined with Lorentzian curve fittings was used for the analysis of the Raman spectra.[43]

II.4 Computational modeling and initial assessments: our crystal modeling is based on the Quantum Espresso (QE) package that includes pressure as an explicit input parameter. We used PBE[44] as the density functional with the Rappe-Rabe-Kaxiras-Joannopoulos ultrasoft pseudopotential[45, 46] and a plane wave basis set with a 47 Ry cutoff. For each pressure between 0 and 18 GPa, we performed full geometry optimization by using the default convergence criteria. For a few models we went up to 36 GPa. We constructed a number of models with the purpose to simulate the main features of the two observed polymorphs (tubular and herringbone). Furthermore, we considered the effects of solvent incorporation, and to a limited degree, the locations of the solvent molecules, whether they occupied an intermolecular region or appeared as guests around the centers of the [6]CPP molecules.

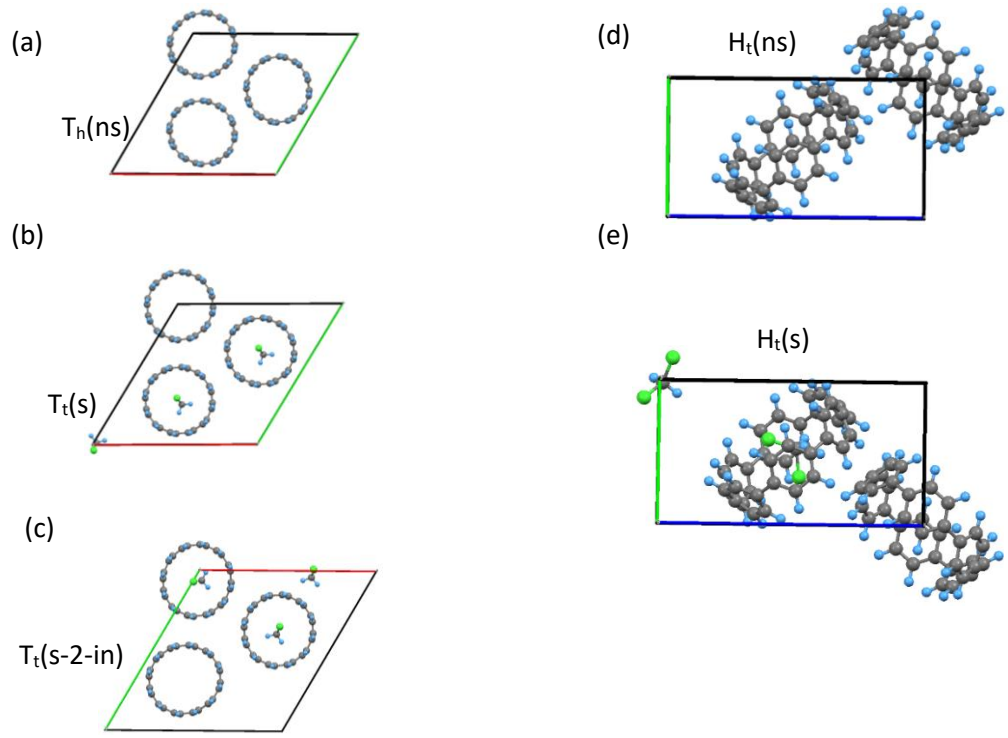

Figure 3. Optimized geometries of (a) T-polymorph solvent-excluded model (Z=3, T_h(ns), top view through the c axis); (b) T-polymorph solvent-included model (Z=3, T_t(s), top view through the c axis); (c) T-polymorph solvent-included model (Z=3, T_t(s-2-in), top view through the c axis); (d) H-polymorph solvent-excluded model (Z=2, H_t(ns), side view through the a axis); (e) H-polymorph solvent-included model (Z=2, H_t(s), side view through the a axis). Carbons are grey, hydrogens are blue and chlorines are green. In the modeling the solvent is dichloromethane as in ref. 39.

The above models belong to these categories:

(i) Tubular-packing (T-polymorph): (Z=3)[10] and is illustrated in Figure 3a. Two forms appear in the modeling, the hexagonal (T_h-polymorph) and the lower symmetry triclinic form (T_t-polymorph).

(ii) Herringbone-packing (H-polymorph): (Z=2) [39] and is illustrated in Figure 3d. Only one form in the modeling, the lower symmetry triclinic form (H_t-polymorph), is considered here.

For both polymorphs we used models with CH_2Cl_2 solvents included (s) and models without solvents (no solvents, ns):
(a) ns models (no solvents): The T_h(ns) model is illustrated in Figure 3a. The other T-polymorph model, T_t(ns) is similar to T_h(ns) except that the symmetry is lower: a≠b. The third model in this group is H_t(ns) which is illustrated in Figure 3d.

(b) s models (with solvents): in the modeling we assume that the ratio of solvent to [6]CPP is 1:1 based on the H-polymorph model.[39] Altogether, we employed three models incorporating solvent molecules:

-- Model T_t(s) contains one solvent molecule are at the center of each [6]CPP as illustrated in Figure 3b.

-- Model T_t(s-2-in) contains two solvent molecules at the centers of two [6]CPPs and the third is located interstitially between the [6]CPPs, as illustrated in Figure 3c.

-- Model H_t(s). For the H-polymorph, we only considered one case, H_t(s), in which all solvents are located at the centers of all [6]CPPs, as shown in Figure 3e.

With the optimized geometries obtained at each P value we calculated the vibrational frequencies (scaled by 0.95) and non-resonant Raman intensities at the frozen geometries with the Gaussian 09 package.[47] We used the B3LYP/6-31G(d) model chemistry with non-resonant Raman intensities. The experimental (at ambient pressure) and computed structures are summarized in Figure 3 and Table 1 for the unit cell and selected molecular parameters. Figure 3 also illustrates the various molecular models used in this work. We note that the three T-polymorph models and the two H-polymorph models agree well with their respective experimental structures at ambient conditions serving as the basis for the high pressure computations. The different polymorphs and their notations in this paper are summarized in Table 2.

Table 1. The geometric parameters of the crystal unit cell of [6]CPP from single XRD and simulated powder XRD patterns compared with the optimized structures of our modeling.

	T-polymorph				H-polymorph		
	Expt. Single XRD (no solvent)[10]	Hexagonal (no solvent) T_h(ns)	Triclinic (no solvent)[a] T_t(ns)	Triclinic (with solvent)[a] T_t(s)	Expt. Simulation from powder XRD (with solvent) [39]	Triclinic (no solvent) H_t(ns)	Triclinic (with solvent) H_t(s)
Z	3	3	3	3	2	2	2
Illustration	Fig. 1a	Fig. 3a	-	Fig. 3b	Fig. 1b	Fig. 3d	Fig. 3e
Axis a /Å	19.3957	20.4133	21.6902	21.2957	11.0988	11.5726	11.6692
Axis b /Å	19.3957	20.4133	21.4183	22.3350	8.2585	8.5304	8.5995
Axis c /Å	6.1998	5.8510	5.8489	5.8382	15.8135	16.4149	16.5428
Angle α /∘	90	90.04	90.59	90.06	89.90	90.09	89.78
Angle β /∘	90	90.04	89.63	90.27	106.91	104.35	104.35
Angle γ /∘	120	120.06	120.06	120.11	90.07	89.89	90.15
Volume / $Å^3$	2019.85	2133.63	2351.68	2402.06	1386.77	1569.88	1608.25
Average Torsion /∘	26.39	0.11	0.36	0.51	27.48	24.42	19.71

Average C_{ortho}-C_{ortho} /Å	1.4900	1.4765	1.4768	1.4767	1.4967	1.4812	1.4823

[a]The structure is nearly hexagonal, but the deviations from hexagonal symmetry are significant.

Table 2. Models and their notations

Model	Solvent	Tubular vs. Herringbone packing	Triclinic vs. Hexagonal	Illustration in Figure
T_h(ns)	no	Tubular	Hexagonal	3a
T_t(ns)	no	Tubular	Triclinic	-
T_t(s)	yes	Tubular	Triclinic	3b
T_t(s-2-in)	yes	Tubular	Triclinic	3c
H_t(ns)	no	Herringbone	Triclinic	3d
H_t(s)	yes	Herringbone	Triclinic	3e

III. RESULTS AND DISCUSSION

In order to facilitate the interpretation of the experimental Raman results and comparison with the computed Raman spectra, we present both sets of data side by side. For this reason, we first discuss the computational molecular structural data of the molecular phases and the new polymeric phases (see Scheme 1 below). Then, we turn to the discussion of the spectra.

III.1 Energy and unit cell volume change with pressure. First, we present the energetics of the T- and H-polymorphs without solvents in Figure 4a and with solvents in Figure 4b, their respective volumes as a function of pressure are shown in Figures 4c and 4d. The presented unit cell energies are relative to the P=0 data. In order to make the data comparable, models without solvents are relative to the T_t(ns) model at P=0, and models with solvent are relative to the T_t(s) models at P=0. The data for the T_h(ns) model (blue crosses) are given in both Figures 4a and 4b, as well as in 4c and 4d in order to provide a basis for comparison.

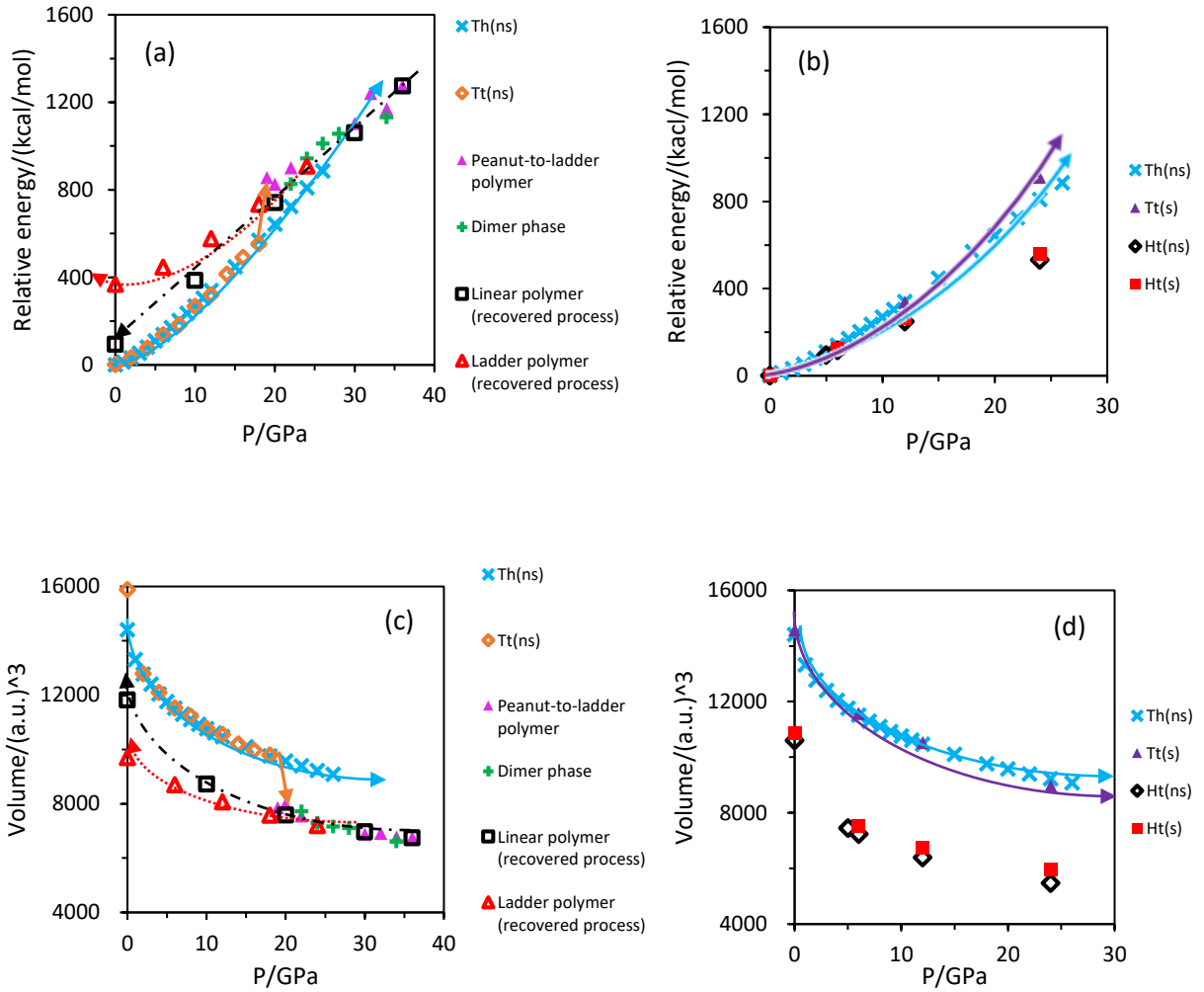

Figure 4. Pressure dependent parameters in the modeling of [6]CPP. (a) and (b) represent the relative total energy per unit cell. (c) and (d) represent the unit cell volume. (a), (c) are from solvent-excluded models; (b) and (d) are from solvent-included models (all solvents are inside of [6]CPPs). Lines are provided to guide the eye, arrows indicate the direction of pressure change. The black and red dashed lines in (a) refer to the recovery process from their respective polymeric phases (see Scheme 1 and Figure 5). The linear polymer phase and the ladder polymer phase appear at ~36 GPa and ~30 GPa, respectively. The orange arrows in (a) and (c) indicate a volume collapse in the T_t(ns) phase at the onset of peanut shapes at ~19 GPa.

Two polymeric phases in Scheme 1 and Figure 5 appear above 22 GPa only in the T-polymorph, one consisting of ladder polymers and the other containing linear polymers. They are identified with their "degree number", defined as the number of chemical bonds connecting one unit with its neighbors.[48] In addition, a dimeric phase also appears at 22 GPa that can be quenched upon releasing pressure to ambient conditions.

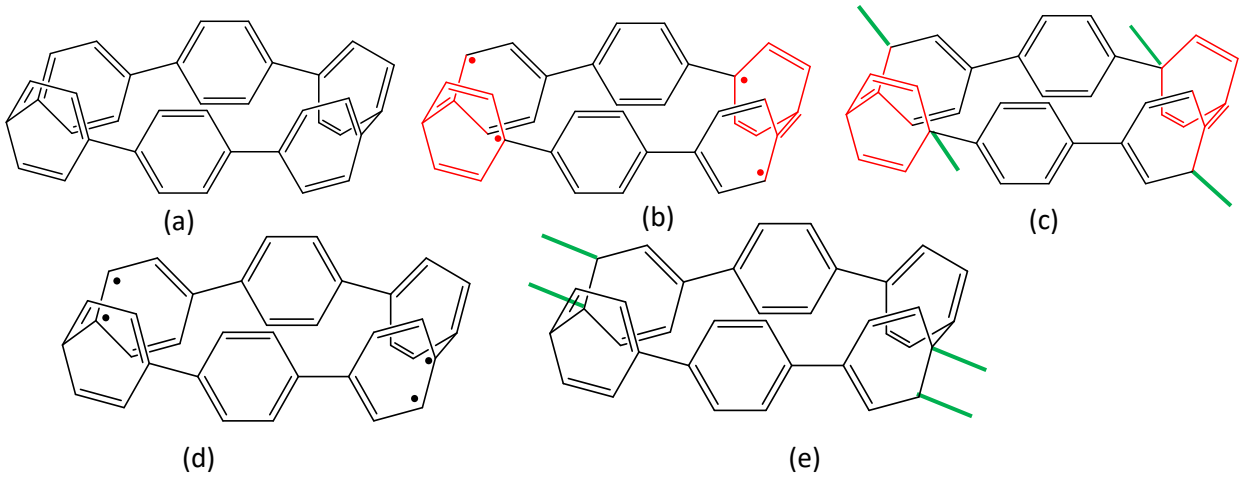

Scheme 1. Two different VB bonding patterns in an isolated [6]CPP: (a) Covalent aromatic structure, and (b) one of the high energy tetra-radicaloid VB structures with partial local quinonoid character. (c) The bonding pattern in a repeat unit of the ladder polymer is closely related to the tetra-radicaloid structure in (b). (d) Another high energy tetra-radicaloid VB structure. (e) The bonding pattern in a repeat unit of the linear polymer is closely related to the tetra-radicaloid structure in (d). Red: quinonoid region, green: bonds in the polymer phases connecting the [6]CPP-derived repeat units. Hydrogens are not shown.

III.1a. Models without solvents (ns). With increasing pressure up to 20 GPa, the molecular crystal structures do not change significantly for the T_h(ns)-polymorph (indicated by the blue crosses in Figure 4a). The energy data for the T_t(ns)-polymorph are very close to the T_h(ns) values because the molecules keep their approximately cylindrical shapes (see empty orange diamonds). The T_h(ns) phase remains cylindrical in all pressures investigated (26 GPa). In contrast, the T_t(ns) phase collapses with a large reduction of the volume and a change to a "peanut" shape pattern occurs as illustrated in Figure S1. The peanut-shaped molecular phase goes up to 22 GPa upon which further pressure increase gives rise to three new phases all involving the formation of new σ-bonds linking vicinal [6]CPP molecules in the unit cell (see magenta triangles in Figure 4a and 4c). Of these three phases, one is dimeric which has the lowest energy (see green crosses in Figures 4a and 4c). The second is a degree-4 ladder polymeric phase (above 30 GPa). The peanut molecular phase and the ladder polymeric phase are indicated by magenta triangles in Figures 4a and 4c. The third new phase has the highest energy and is a degree-4 linear polymeric phase denoted by empty black squares. The recovery processes of the ladder polymer phase (empty red triangle) and linear polymer phase (empty black square) are highlighted by additional red and black dashed lines, respectively. These two polymers retain their newly formed σ-bonds in the pressure release process, however, the energies at ambient pressure are much higher compared to the pristine molecular phase, or kinetic products. The new phases contain more chemical bonds, and they display highly strained structures with a loss of conjugation compared to the original molecular [6]CPP. The ovalization process upon increasing pressure is mild but once a peanut shape is formed, further squeezing gives rise to either a σ-bonded dimer or a ladder polymer with partial local quinonoid character (Scheme 1c).

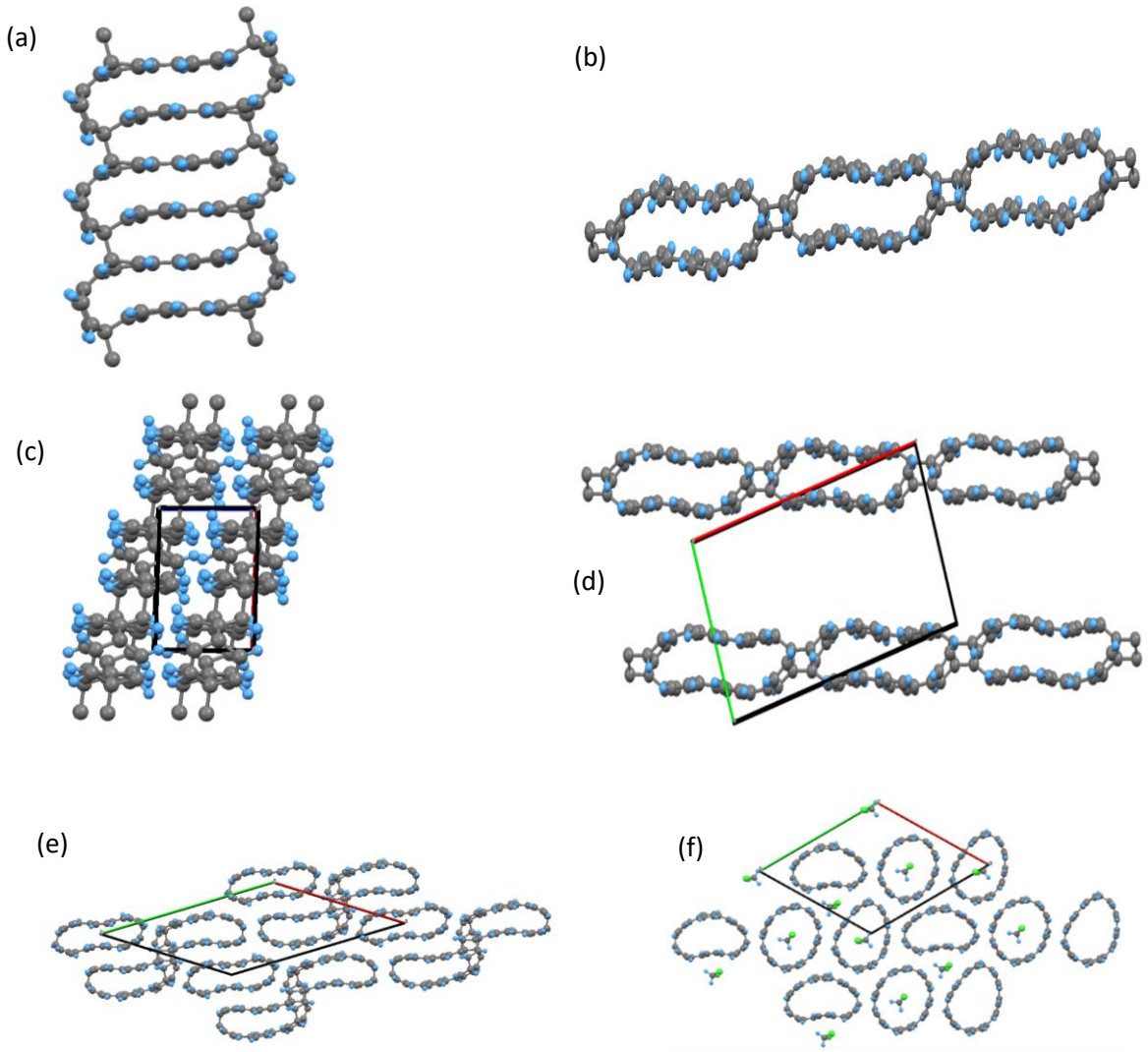

Figure 5. Three types of aggregates found in the high pressure modeling of [6]CPP. (a) Three units of the ladder polymer at P=30 GPa; (b) Three units of the linear polymer that starts to appear at P=36 GPa; (c) The side view of a unit cell of (a) through b axis; (d) The side view of a unit cell of (b) through c axis; (e) Four periodic units of dimeric phase at P=20 GPa through *a* axis; (f) Four units of T_t(s-2-in) at P=12 GPa. Solvents are dichloromethane molecules.[39] Carbons are grey, hydrogens are blue and chlorines are green.

III.1b. Models with solvents (s). The overall phase behavior of the solvent-included models is simpler because the [6]CPPs resist deformation if a well-fitting solvent molecule is encapsulated. In Figure 4b and 4d, blue crosses represent T_h(ns) which are included for comparison. The purple triangles of T_t(s) represent T-polymorph triclinic crystal with solvents, red square of H_t(ns) represents H-polymorph triclinic crystal without solvents and empty black diamond of H_t(s) represents H-polymorph triclinic crystal with solvents. We note that the crossing of the T_h(ns) and the T_t(s) curves occurs above 12 GPa in Figure 4b and above this crossing point significant changes of the unit cell parameters occur in the 12-15 GPa range as shown in Figures S2c and S2d. However, comparing the H_t(ns) and H_t(s) models with respect to the changes of the energy, volume and unit cell parameter as a function of pressure, we observe negligible differences between solvent-included and excluded situations. This demonstrates that pressure has limited influence on solvents in the H-polymorph within the pressure range investigated.

III.2 Molecular structural changes with pressure. The two most significant crystal lattice parameters which are particularly sensitive to pressure are those defined as *a* and γ in Figure S2. It must be noted that the peanut shaped structures (i.e., magenta triangles in Figures S2a and S2b) represent the starting point of a collapse in the increasing pressure direction. This observation explains the deviation of the energy of the T_t(ns) phase from the T_h(ns) phase in Figure 4a.

As already shown, Scheme 1 and Figure 5 illustrate the molecular building blocks of the polymeric phases discovered during our high pressure simulations. In particular, Schemes 1b and 1d display the bonding patterns of tetra-radicals from valence bond (VB) structures derived from the closed-shell full bonding structure of Scheme 1a. These three can be viewed as the precursors of the degree-4 polymers drawn in Scheme 1c and 1e. In the mechanochemical event, these radical sites are connected and develop into intermolecular σ-bonds. The red regions in Scheme 1b and 1c show quinonoid characteristics which have a large negative contribution to the average BLA shown in Figure 6a. In addition to the two polymeric phases the new dimeric phase, illustrated in Figure 5e, exhibits a multiply σ-bonded carbon cage between adjacent [6]CPP molecules whereby only two molecules out of three in one unit cell participate in this complex bond formation. All three molecules remain in a general peanut-like shape. Figure 5f illustrates the structural distortion when two solvent molecules occupy the centers of two [6]CPPs, while the third occupies an intermolecular void space. The earlier emergence of peanut-like shape shown in Figure 5f and Table S1 demonstrates that interstitially filled solvent molecules provoke the cylindrical structure to collapse at a lower pressure (~ 12 GPa) compared to the empty [6]CPP (~ 19 GPa). Since the experimental single X-ray diffraction is affected by disorder, experimentalists concluded[10] that the structure of the samples likely contains a combination of different solvent positions. Previous XRD analysis was unsuccessful to determine the location or the number of solvent molecules in the unit cell due to disorder.

In addition to the directly computed values of energy, volume and unit cell parameters, the following geometrical indicators (average bond length alternation (BLA), torsion (θ) and flattening factor *f*(P), are useful to describe the deformation of the molecular shape as a function of pressure. The BLA values are computed from the r, r_1, r_1' and r_2 values as defined in eq. (1), and they clearly reflect the aromatic vs. quinonoid nature of [6]CPP which, in turn, depend on a combination of factors such local π-conjugation, torsion and bending angles defined in Figure S3. Figures 6a and 6d present the trends of BLA upon increasing pressure. Both solvent included or excluded models display a similar trend moving from the more aromatic structures toward the more quinonoid ones but at different rates. Interestingly, the peanut-shaped molecule (magenta triangle below 22 GPa) in Figure 6a shows a dramatic drop in BLA that we attribute to the relatively flat surface of the phenyl units parallel with the major axis in the peanut-shaped [6]CPP with shorter C_{ipso}-C_{ispo} distances. In the solvent-included models, both T- and H-polymorph phases have a lower BLA above 6 GPa compared to their solvent excluded counterparts (shown in Figure 6d). This observation suggests that in real samples the structure with solvents should be further squeezed toward the quinonoid direction.

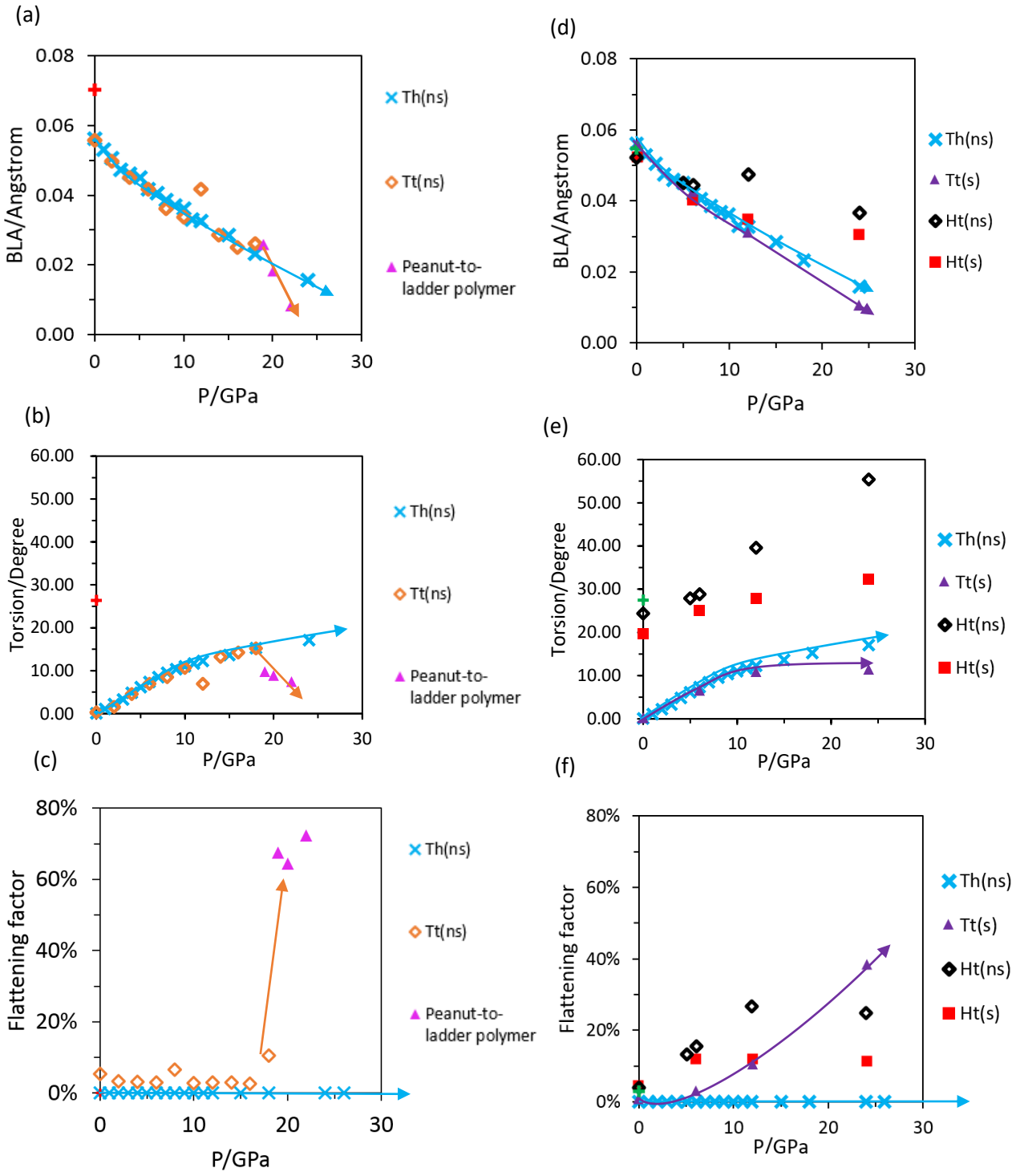

Figure 6. Geometrical parameters as a function of pressure for [6]CPP. (a) and (d) show average bond length alternations (BLA). (b) and (e) show average torsions (θ). (c) and (f) show flattening factors *f*(P). (a), (b), and (c) in the left column are based on solvent-excluded models and (d), (e), and (f) in the right column are based on solvent-included models (all solvents are inside of [6]CPPs). At P=0.1 MPa the red crosses are from the experimental single XRD[10] and the green crosses are from the simulated powder XRD[39]. Lines are provided to guide the eye, arrows indicate the direction of pressure change.

The average torsion in Figures 6b and 6e provides a qualitatively inverse response to pressure compared to BLA. In the other words, the torsion gradually increases upon increasing pressure for all models (solvent-excluded and -included) except for the peanut-shaped molecule which has extremely short interring bonds and flat surfaces parallel with the major axis (see discussions above). These small torsions in the peanut-shaped molecules are in line with the development of shortened $C_{ispo} – C_{ispo}$ bonds. Accordingly, the intra-benzene bonds also shift toward an overall quinonoid structure under high pressure, which is also consistent with the smaller BLA values seen in Figure 6a. At the same time, solvent-included models always show a smaller torsion which agrees well with the smaller BLA in the solvent include models compared to the solvent excluded models in Figure 6d.

Dramatic differences between solvent-excluded and solvent-included models are shown in the flattering factor diagram of Figures 6c and 6f. In Figure 6c, before the appearance of peanut shape, both T_h(ns) and T_t(ns) models display approximately cylindrical shapes with flattening factor values near zero. On the other hand, in Figure 6f, a larger deformation toward an elliptical shape emerges for filled [6]CPP at a pressure as low as 12 GPa, indicating that voids occupied by solvents significantly change the surrounding environments and the strains of the [6]CPP molecules in the T polymorphs. For the H polymorphs the effect of solvent on ovalization is smaller and acts in the opposite direction, which is to say that a filled [6]CPP prevents the ovalization indicated by a smaller flattening factor. In addition, T_t(s-2-in) shown in Figure 5f displays a higher degree of deformation from oval to peanut-like shape, compared to T_t(s) in Figure 6f, which initiates the formation of σ-bonds and aggregation at a lower pressure. (See Table S1.).

The increase in the flattening factor upon pressure shows that the approximately cylindrical shape of the [6]CPP molecules undergoes a reduction of symmetry resulting in the splitting of several vibrational modes. This splitting into sub-bands is a major general feature of the observed pressure effect in the molecular phase and is seen in both the computations and the Raman experiments. It is important to note that in the low pressure regime where Raman data are available, the solvent included and excluded models behave very similarly in terms of shapes and molecular phases and no new σ-bonds are formed in any of these models within the pressure range investigated. Therefore, in the following Raman frequency analysis, we mainly use solvent-excluded models to simulate the experimental vibrational data, although for comparison we also have limited data with the T_t(s) solvent-included model.

III.3 Raman spectra as a function of pressure. The discussion of the Raman spectrum will be divided into several regions from 220 to 1650 cm^{-1}. Figure 7 shows the main experimental Raman bands and the assignments of the important bands at P=0.1 MPa given in Table S2.[48] Both the average absolute deviation and the root-mean-square deviation values demonstrate that all three models, T_h(ns), T_t(ns) and T_t(s), produce Raman frequencies that are closer to the experimental values than from computations on the isolated molecule in vacuum. This indicates that the intermolecular interactions play an important role even at ambient conditions. We take this as a fundamental justification to use our solid state models to analyze the pressure dependent Raman frequencies.

Figure 7 contains the experimental Raman spectra at selected pressures. Starting from the bottom, the first nine spectra show the effects of increasing pressure while the top one corresponds to the condition where the pressure is released from the maximum of P=7.2 GPa and is reduced back to ambient P=0.1 MPa.

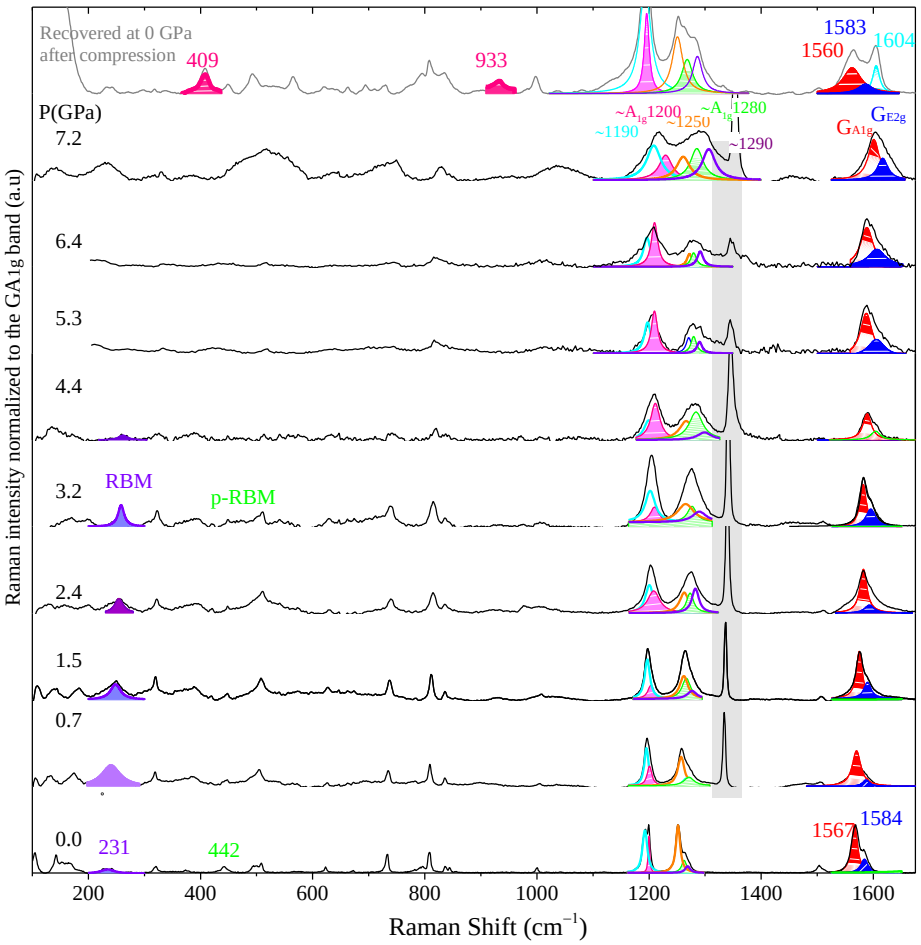

Figure 7. The experimental Raman spectra of [6]CPP at selected pressures, increasing pressure from bottom to top. The very top spectrum corresponds to the recovered sample after decompression from 7.2 GPa. Colored areas correspond to Lorentzian fitting of the bands. Purple low frequency bands are assigned to the RBM, green low frequency bands to the p-RBM modes. In the high wavenumber regions, the G_{A1} and G_{E2} are represented as red and dark blue areas, respectively. The grey area represents the pressure calibration peak.

III.3.1 General spectroscopic findings. Overall, the bands remain well identifiable although the overall trend of broadening with increasing pressure is significant, especially in the 1100-1350 cm^{-1} region. However, bands in the low frequency region (220-900 cm^{-1}) broaden to the extent that they lose the characteristic CPP peaks such as the radical breathing mode (RBM) and the pseudo-PRM (p-RBM).[16] The high pressure treatment of the samples clearly lacks reversibility once reaching 7.2 GPa. For example, new bands at 409 and 933 cm^{-1} appear in the recovered sample (see dark pink shaded peaks in Figure 7). It is important to note that the spectra are fully reversible up to ~4 GPa and then the irreversible behavior starts at about 5 GPa. Figure 8 compares the Raman frequencies from the experiment and three different theoretical models, T_h(ns), T_t(ns) and T_t(s), as a function of pressure. Both experiment and modeling show significant band splitting due to the loss of symmetry in the crystal as the pressure is increased beyond 1-2 GPa. In the experimental data, especially in the low frequency region, the Raman bands become difficult to identify due to the increasing spectral background with increasing compression. Therefore some of the

lines stop at various pressure values. Of course, this is not the case for the computed frequencies, because all modes remain identifiable even though their intensities can be very small.

Black straight lines in Figure 8 are provided to guide the eye to emphasize the changes in the derivatives (slopes) of the Raman frequency shifts with respect to pressure. The particular regions of pressure around 5 GPa, where the slopes change significantly are the same for all Raman peaks. In the computations this region of slope change, as indicated by the intersection of the black straight lines, varies from model to model and also independent of frequency. The slope changes occur around 5 GPa for the T_h(ns) model and around 6 GPa in the T_t(ns) model. For the solvent-included T_t(s) model the pressure at which the slopes change spreads over a wider range at around 9 GPa. The slope changes are observed at around 5 GPa in the experiments, in good agreement with the T_h(ns) and T_t(ns) models.

III.3.2 Changes in the low frequency spectral region (200-525 cm^{-1} and 650-900 cm^{-1}). The frequency variation with pressure in this region is represented in Figure 8. In particular, the frequency of the lowest band (RBM) together with the band near 450 cm^{-1} increases with respect to pressure in a similar pattern. These two bands agree well with one another in the three models and they correspond well to the experiment. The third band near 500 cm^{-1} (RFM, radical flexural mode) in the experiment shows some small variations, while the calculations, according to all three models, show also modest variations. Similarly, the bands near 700 and 800 cm^{-1} in the theory have positive slopes which represent the experimental slopes quite well. Meanwhile the experimental band near 840 cm^{-1} has an almost zero slope but our calculation obtained a small negative slope. Another difference in the calculations with respect to the experiments is the emergence of multiple sub-bands below 800 cm^{-1} in the models. Such bands become more outstanding when P is larger than 4 GPa. For the bands in the 750 to 850 cm^{-1} region we note a dramatic change of slopes toward negative starting from 7-8 GPa in all models, but unfortunately there are no experimental data to compare them with due to the overwhelming background.

III.3.3 Changes in the medium frequency spectral region (1160-1400 cm^{-1}). In this region two sets of bands are present (~1200 and ~1260 cm^{-1}) and their intensity ratio is closely related to the pressure which is shown in Figure S4.[16] The loss of symmetry and broadening of bands also start at ~6 GPa, exhibiting a smaller slope after the intersection of the black lines in Figure 8 without exception. Some slopes of both sets in the experiment show negative values after the intersection (~6 GPa) while the slopes in the theoretical model only display nearly zero values but never negative ones.

III.3.4 Changes in the high frequency spectral region (1400-1600 cm^{-1}). The highest frequency region includes two main vibrational modes (G_{A1} and G_{E2}) which are strongly coupled to the BLA[16,41] and are drawn in red and blue 1567 cm^{-1} and 1584 cm^{-1} in Figure 7, respectively. Our previous study of [n]CPP at ambient pressure[16] interpreted that the Raman frequencies of these bands are directly related to the BLA, and thus to the degree of the aromatic *vs*. quinonoid character of the CPP.[49,50] The computed initial frequencies at ambient pressure shown in Table S2 and Figure S5 reproduce the experimental data well. The slopes of two main bands (1570 and 1590 cm^{-1}) in the models become smaller after the intersections of black lines which occur at various pressure values: ~5 GPa in the T_h(ns) model, ~6 GPa in the T_t(ns) model and ~9 GPa in T_t(s) model. No broadening is observed experimentally or theoretically in this high frequency region due to the high symmetry of [6]CPP molecule shown by the small flattening factors in Figure 6c. The transformation from an aromatic toward a quinonoid structure appears at around 5 GPa in the experiment and at somewhat higher pressures in the computational modeling as indicated by Figure 8. We will comment on these differences at the end.

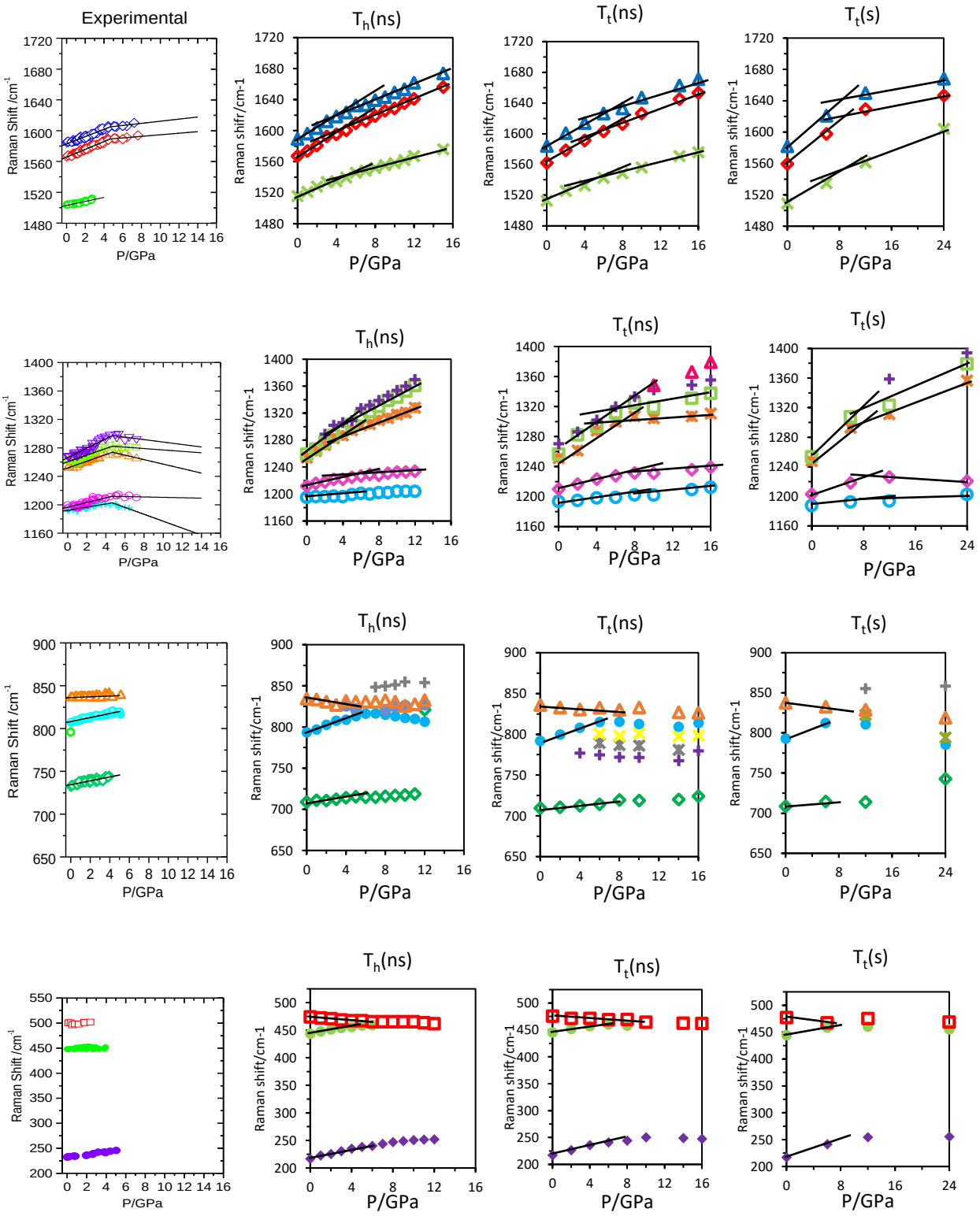

Figure 8. Raman frequencies of [6]CPP as a function of pressure. Experimental (left column) and computed (second column: T_h(ns) model; third column: T_t(ns) model; fourth column: T_t(s) model).

In general, for the whole Raman spectral region studied, Table 3 presents the comparison of the derivatives of the Raman shifts with respect to pressure for selected peaks from the experiments and four theoretical models. Most of these slopes range from -1 to 8 cm^{-1}/GPa. The computed models predict overall larger slope values by about 50% in the 1252-1504 cm^{-1} range and about 30% larger values for the bands at 1567 and 1584 cm^{-1} compared to the experiment. By comparing the slopes of three models of the T-polymorph, we find that the T_t(ns) model has the best prediction. Figure S6 provides a comparison of the three models of the T-polymorph and one of the H-polymorph, which shows that the H_t(s) model provides a good correlation with the experimental Raman shift derivatives. . We note that the experiments start with the T structure at ambient pressure and Raman spectra are available only for the T-polymorph. Further information on the H-phases can be found in Figure S7.

Table 3. The initial (P=0) derivatives of pressure dependent Raman frequencies for [6]CPP (in cm^{-1}/GPa).

Experimental frequency at P=0.1 MPa (in cm^{-1})	Expt.[a]	Theor. T_h(ns) model[b]	Theor. T_t(ns) model[c]	Theor. T_t(s) model [d]	Theor. H_t(s) model[d]
231	2.6±0.1	3.9	3.4	4.1	1.5
442	0.3±0.3	2.6	1.6	2.3	1.1
505	0.6±0.1	-1.4	-0.8	-1.6	0.3
734	1.9±0.2	1.0	1.2	1	0.4
805	2.4±0.2	3.8	3.1	3.3	0.3
836	0.5±0.2	-0.6	-0.6	-0.9	-0.5
1193	2.3±0.2	0.9	1.1	0.8	0.03
1200	3.3±0.2	2.4	2.7	2.6	0.7
1252	4.7±0.2	7.9	7.5	7.5	4.4
1263	4.7±0.2	9.3	8.3	9	5.9
1269	6.6±0.2	8.3	8.0	-	7.4
1504	2.6±0.2	4.8	4.4	4.3	2.3
1567	5.1±0.2	6.9	6.3	6.4	4.6
1584	4.7±0.2	7.1	6.2	6.5	3.9
Average absolute deviation for 14 slopes		1.94	1.44	1.77	0.93
Root-mean-square deviation (RMSD) for 14 slopes		2.17	1.65	1.92	1.13

[a] The average slope is calculated for the region 0~4.7 GPa.
[b]The average slope is calculated for the region 0~5 GPa.
[c] The average slope is calculated for the region 0~6 GPa.
[d] The average slope is calculated for the region 0~8 GPa.

The derivatives of the Raman frequency shifts with respect to pressure are directly related to the mode Grüneisen parameters (γ_i) as discussed in the literature for both internal and external vibrational modes of molecular materials under high pressure [51] and are linked to local volume changes and anharmonicities of the modes. [36, 52,53] These γ_i parameters are discussed in the Supporting Information section in connection with Figure S8. In addition, the most striking observation is that the negative slopes

of the RFM mode shown in Figure S8 suggest an instability of the molecular shape of the nanohoop with increasing compression. In order to characterize the electronic properties of the high pressure phases in the solid state, we also computed the bandgaps of two models and the respective data are shown in Figure S9 which indicates a dramatic drop of the gap at P=19 GPa in accordance with the appearance of the peanut shaped strained molecules. No dramatic electronic structure changes are indicated within the experimental range, and the decrease of bang gap with respect to pressure demonstrates the geometry change from the aromatic to the quinonoid structure.

III.3.5 Chemical or phase irreversibility from the Raman data. A particularly important question is the reversibility of the Raman shifts or lack thereof upon the release of pressure. The spectra are nearly perfectly reversible for pressures up to 5 GPa. The Raman spectrum recovered from a pressure treatment at 7.2 GPa is shown on the top of Figure 7 indicating the appearance of new bands and other significant changes. While we are unable to provide a detailed quantitative explanation for the causes of this irreversibility from other experimental techniques, we provide an alternative interpretation based on our modeling.

Based on our modeling, there are two steps before aggregation or σ-bond formation. Step one is the ovalization which is enhanced by the presence of solvent molecules shown in Table S1. Step two is the collapse (the appearance of peanut shape) where empty [6]CPP is easier to further squeeze Our calculations showed that the compressed molecular phase (even with the peanut shape) can return to the pristine structure in the molecular phase when pressure is released. Once new bonds are formed (such as the σ-bonded dimer, or the two types of degree-4 polymers) these [6]CPP chemical aggregates retain their new bonds as pressure is reduced back to ambient pressure. These two transitions (ovalization before collapse and aggregation after collapse) correspond to the two critical pressures observed (P=5 GPa where the slope changes, and P=7.2 GPa where complete irreversibility occurs) in the experiment. From the comparison between the shapes of the cross section of nanohoops in three models T_t(ns), T_t(s) and T_t(s-2-in) shown in Table S1, the surprising conclusion is that the solvent molecules lower the ovalization pressure. This means that the ovalization as well as the subsequent collapse and aggregation occurs at a lower pressure.

A similar irreversible aggregate formation was also seen in our high pressure study of [5]CPP.[54] Thus, we argue that the irreversibility comes from the formation of new σ-bonds upon large compressions. There is an obvious discrepancy with respect to experiment (ca. 7.2 GPa) in the onset of this aggregation since the onset of the formation of the aggregates is predicted at about 22 GPa for dimer formation and 30 - 36 GPa for polymer formation in the T_t(ns) model. Real [6]CPP nanohoops in the sample have an disordered distribution of solvent molecules, and the interstitially located solvent is more effective in deforming the adjacent [6]CPPs leading to a lower ovalization and aggregation pressure shown in Table S1. In fact, the collapse to the peanut shape in T_t(s-2-in) model emerges at a lower pressure at 12 GPa compared to 19 GPa in T_t(ns) model, and these peanut-shaped molecules are easy to be deformed into aggregates upon further pressure. Accordingly, a reasonable inference about the effect of solvents is that additional uneven distribution of the interstitial solvents creates large local deformations and lowers the aggregation pressure significantly.

The ovalization pressures from the experiment and modeling agree reasonably well. However, the onset of aggregation appears experimentally at a much lower pressure than in any of the models. In order to resolve this discrepancy, two effects should be considered. A smaller factor is due to the possible

appearance of non-hydrostatic conditions in the experiments, so higher local pressures required to trigger the aggregate formation may be present in the sample compared to the nominal hydrostatic pressure. A more important factor in the case of [6]CPP is the uneven disordered distribution of the solvent molecules especially those interstitially located in the sample, in contrast to the modeling where perfect periodic boundary conditions are imposed.

IV. CONCLUSIONS

In this combined experimental Raman spectroscopic and computational study we explored the structural changes and vibrational properties of a cyclic nanohoop molecule, [6]CPP, under high pressures. Inspired by the structures of the two known polymorphs (T and H), we modeled both polymorphs under high pressures with consideration for the inclusion of solvent molecules. Our modeling represents frequency shift derivatives with respect to pressure within the low pressure range up to ~5 GPa which is in good agreement with our experiments. We identified this pressure as the beginning of significant ovalization of the tubular packed [6]CPP nanohoops. After this ovalization pressure the derivatives of the Raman shifts decrease to smaller positive values, or become even negative for some modes. This trend is also reproduced in our modeling, with slightly larger ovalization pressure values for different models. We analyzed the geometrical changes of the [6]CPP in the molecular phase upon pressure by monitoring their BLA, interring torsion and the flattening factors, providing structural explanations for the trends in the spectra. In agreement with earlier work on [n]CPPs at ambient pressures as a function of n, and for [5]CPP as a function of pressure, we correlate the changes of the BLA with a general switch from aromatic to quinonoid structure in [6]CPP.

During modeling we discovered three novel phases of [6]CPP containing chemical aggregates at pressures above the experimental range: one dimeric and two polymeric phases. All these phases remain quenched in the aggregated phase once the pressure is released. The aggregate formation is facilitated by inclusion of solvent molecules into [6]CPP and especially interstitial located solvents create a lower aggregation pressure compared to the empty [6]CPP. Empty [6]CPPs attain highly deformed peanut-like shapes before forming σ-bonded aggregates and the aggregated forms remain after the pressure is released in our modeling. These models without solvents together with the solvent induced effects shown by the filled models provide a strong basis for explaining the irreversibility observed in the Raman spectra beyond 7.2 GPa. Modeling and experiment differ in the onset pressure for this irreversibility, and we argue that this is likely due to the disordered distribution of solvent molecules in the experiment, as they can reside inside or between [6]CPPs or even be randomly absent in different locations of the material.

The critical pressures both in theory and experiment do not depend on the vibrational mode. This commonality of the critical pressure where the slopes of the Raman frequency shifts change is a key feature of the molecular phase and lends strong support to the interpretation based on the underlying structural changes that involve ovalization, benzene-benzene torsion and most importantly changes of the bond length alternation. The latter is particularly essential as indicated by previous work on paraphenylenes.[16, 41, 48] In conclusion, this work demonstrates that in combination with modern DFT solid state calculations, Raman spectroscopy is an effective tool to provide atomistic level descriptions of complex organic molecules and their pressure-induced reactivity as well as other mechanochemical effects.

Acknowledgements

We thank the U. S. National Science Foundation for its support of this research at Georgetown University (grant number CHE-1006702). Financial support from MINECO, Government of Spain is acknowledged (project reference FEDER CTQ CTQ2015-69391-P). This work has been also supported by MINECO through the projects CSD2007-00045, CTQ2012-38599-C02-02 and CTQ2013-48252-P. MPA is grateful to the Spanish Ministerio de Educación, Cultura y Deporte for an FPU grant.

References:

[1] B. Chen, R. Hoffmann, R. Cammi, *Angew. Chem. Int. Ed.* 2017, *56*, 11126.
[2] N. V. Plotnikov, T. J. Martinez, *J. Phys. Chem. C* **2016**, *120*, 17898.
[3] Y. Ren, S. Lee, J. M. Christensen, N. V. Plotnikov, M. Burgess, T. J. Martinez, D. D. Dlott, J. S. Moore, *Chem. Mater.* **2016**, *28*, 6446.
[4] M. T. Ong, J. Leiding, H. Tao, A. M. Virshup, T. J. Martinez, *J. Am. Chem. Soc.* **2009**, 131 (18), 6377 – 6379.
[5] J. M. Lenhardt, J. W. Ogle, M. T. Ong, R. Choe, T. J. Martinez, S. L. Craig, *J. Am. Chem. Soc.* **2011,** 133 (10), 3222-3225.
[6] G. Subramanian, N. Mathew, J. Leiding. *J. Chem. Phys.* **2015** ,143 (13), 134109.
[7] M. Krupicka, P. Dopieralski, D. Marx, *Angew. Chem. Int. Ed.* **2017**, 56, 7745-7749.
[8] M. Dresselhaus, G. Dresselhaus, P. Avouris, *Springer, Berlin*, **2001.**
[9] R. Jasti, J. Bhattacharjee, J. B. Neaton, C. R. Bertozzi, *J. Am. Chem. Soc.* **2008**, *130*, 17646.
[10] J. Xia, R. Jasti, *Angew. Chem. Int. Ed*. **2012**, *51*, 2474.
[11] P. J. Evans, E. R. Darzi, R. Jasti, *Nat. Chem.* **2014**, *6*, 404.
[12] H. Omachi, S. Matsuura, Y. Segawa, K. Itami, *Angew. Chem., Int. Ed*. **2010**, *49*, 10202.
[13] E. Kayahara, T. Iwamoto, T. Suzuki, S. Yamago, *Chem. Lett*. **2013**, *42*, 621.
[14] E. Kayahara, V. K. Patel, J. Xia, R. Jasti, S. Yamago, *Synlett.* **2015**, *26,* 1615.
[15] Y. Segawa, A. Fukazawa, S. Matsuura, H. Omachi, S. Yamaguchi, S. Irle, K. Itami, *Org. Biomol. Chem*. **2012**, *10,* 5979.
[16] M. Pena-Alvarez, L. Qiu, M. Taravillo, V.G. Baonza, M.C.R. Delgado, S. Yamago, R. Jasti, J.T.L. Navarrete, J. Casado, M. Kertesz, *Phys. Chem. Chem. Phys*. **2016**, *18*, 11683.
[17] M. Fujitsuka, D. W. Cho, T. Iwamoto, S. Yamago, T. Majima. *Phys. Chem. Chem. Phys*. **2012**, *14*, 14585.
[18] T. Nishihara, Y. Segawa, K. Itami, Y. Kanemitsu, *Chem. Sci*. **2014**, *5*, 2293.
[19] M. Talipov, R. Jasti, R. J. Rathore, *J. Am. Chem. Soc*. **2015**, *137*, 14999.
[20] E. Kayahara, T. Kouyama, T. Kato, H. Takaya, N. Yasuda, S. Yamago, *Angew. Chem. Int. Ed*. **2013**, *125*, 13967.
[21] T. Iwamoto, Y. Watanabe, T. Sadahiro, T. Haino, S. Yamago, *Angew. Chem. Int. Ed.* **2011**, *123*, 8492.
[22] Y. Nakanishi, H. Omachi, S. Matsuura, Y. Miyata, R. Kitaura, Y. Segawa, K. Itami, H. Shinohara, *Angew. Chem. Int. Ed*. **2014**, *53*, 3102.
[23] T. Iwamoto, Z. Slanina, N. Mizorogi, J. Guo, T. Akasaka, S. Nagase, H. Takaya, N. Yasuda, T. Kato, S. Yamago, *Chem. Eur. J*. **2014**, *20*, 14403.
[24] G. Povie, Y. Segawa, T. Nishihara, Y. Miyauchi, K. Itami, *Science,* **2017**, *356***,** 172.
[25] S. Nishigaki, M. Fukui, H. Sugiyama, H. Uekusa, S. Kawauchi, Y. Shibata, K. Tanaka. *Chem. Eur. J*. **2017**, *23*, 7227.
[26] M. Sakurai, S. Saito. *Physica E: Low-Dim. Systems Nanostruct.* **2011**, *43*, 673.
[27] M. Nicol, G.Z. Yin, *J. de Physique Coll.* **1984**, 45, C8-163-C8-172.

[28] X.D. Wen, R. Hoffmann, N.W. Ashcroft, *J. Am. Chem. Soc.* **2011**, 133(23), 9023-9035.
[29] B. Chen, R. Hoffmann, N. W. Ashcroft, J. Badding, E. Xu, V. Crespi, *J. Am. Chem. Soc.* **2015**, 137, 14373–14386.
[30] T. C. Fitzgibbons, M. Guthrie, E.S. Xu, V. H. Crespi, S. K. Davidowski, G. D. Cody, N. Alem, J. V. Badding, *Nat. Mater.* 2015, 14, 43–47
[31] M. Hanfland, A. Brillante, K. Syassen, M. Stamm, J. Fink, *J. Chem.Phys*. **1989**, 90, 1930.
[32] (a) S. Guha, W. Graupner, R. Resel, M. Chandrasekhar, H.R. Chandrasekhar, R. Glaser, G. Leising, *J. Phys. Chem. A* **2001**, *105*(25), 6203-6211.
(b) C. M. Martin, Q. Cai, S. Guha, W. Graupner, M. Chandrasekhar, H. R. Chandrasekhar, *Phys. Stat. Sol.* **2004**, 241, 3339−3344.
[33] M. Oehzelt, A. Aichholzer, R. Resel, G. Heimel, E. Venuti, R.G. Della Valle, *Phys. Rev. B* **2006**, 74(10), 104103.
[34] G. Heimel, P. Puschnig, M. Oehzelt, K. Hummer, B. Koppelhuber-Bitschnau, F. Porsch, C. Ambrosch-Draxl, R. Resel, *J. Phys. Condens. Matter* **2003**, 15(20), 3375.
[35] G. Heimel, K. Hummer, C. Ambrosch-Draxl, W. Chunwachirasiri, M.J. Winokur, M. Hanfland, M. Oehzelt, A. Aichholzer, R. Resel, *Phys. Rev. B* **2006**, 73(2), 024109.
[36] M. Knaapila, S. Guha, *Rep. Progr. Phys*. **2016**, *79*, 066601.
[37] A. N. Imtani, V. K. Jindal, *Comput. Mater. Sci.* **2009**, *46*, 297.
[38] A. L. Aguiar, R. B. Capaz, A. G. S. Filho, A. San-Miguel, *J. Phys. Chem. C.* **2012**, *116*, 22637.
[39] T. Fukushima, H. Sakamoto, K. Tanaka, Y. Hijikata, S. Irle, K. Itami, *Chem. Lett.* **2017**, *46*, 855.
[40] M. Kertesz, C. H. Choi, Y. S. Yang, *Chem. Rev*, **2005**, *105*, 3448.
[41] G. Zannoni, G. Zerbi, *J. Chem. Phys*. **1985**, *82*, 31.
[42] V. G. Baonza, M. Taravillo, A. Arencibia, M. Cáceres, J. Nunez, *J. Raman Spectrosc*. **2003**, *34*,264.
[43] E. Del Corro, M. Taravillo, J. González, V. G. Baonza, *Carbon*, **2011**, *49*, 973.
[44] P. Giannozzi, S. Baroni, N. Bonini, M. Calandra, R. Car, C. Cavazzoni, D. Ceresoli, G. L. Chiarotti, M. Cococcioni, I. Dabo, A. Dal Corso, S. Fabris, G. Fratesi, S. de Gironcoli, R. Gebauer, U. Gerstmann, C. Gougoussis, A. Kokalj, M. Lazzeri, L. Martin-Samos, N. Marzari, F. Mauri, R. Mazzarello, S. Paolini, A. Pasquarello, L. Paulatto, C. Sbraccia, S. Scandolo, G. Sclauzero, A. P. Seitsonen, A. Smogunov, P. Umari, R. M. Wentzcovitch, *J. Phys. Condens. Matter*, **2009**, *21*, 395502.
[45] We used the pseudopotentials C.pbe-n-rrjkus_psl.UPF and H.pbe-rrkjus_psl.UPF from the Quantum ESPRESSO pseudopotential data base: http://www.quantum-espresso.org/pseudopotentials.
[46] A. M. Rappe, K. M. Rabe, E. Kaxiras, J. D. Joannopoulos, *Phys. Rev. B*, **1991**, *44*, 13175.
[47] Gaussian 09, Revision D.01, M. J. Frisch, G. W. Trucks, H. B. Schlegel, G. E. Scuseria, M. A. Robb, J. R. Cheeseman, G. Scalmani, V. Barone, B. Mennucci, G. A. Petersson, H. Nakatsuji, M. Caricato, X. Li, H. P. Hratchian, A. F. Izmaylov, J. Bloino, G. Zheng, J. L. Sonnenberg, M. Hada, M. Ehara, K. Toyota, R. Fukuda, J. Hasegawa, M. Ishida, T. Nakajima, Y. Honda, O.Kitao, H. Nakai, T. Vreven, J. A. Montgomery, Jr., J. E. Peralta, F. Ogliaro, M. Bearpark, J. J. Heyd, E. Brothers, K. N. Kudin, V. N. Staroverov, R. Kobayashi, J. Normand, K. Raghavachari, A. Rendell, J. C. Burant, S. S. Iyengar, J. Tomasi, M. Cossi, N. Rega, J. M. Millam, M. Klene, J. E. Knox, J. B. Cross, V. Bakken, C. Adamo, J. Jaramillo, R. Gomperts, R. E. Stratmann, O. Yazyev, A. J. Austin, R. Cammi, C. Pomelli, J. W. Ochterski, R. L. Martin, K. Morokuma, V. G. Zakrzewski, G. A. Voth, P. Salvador, J. J. Dannenberg, S. Dapprich, A. D. Daniels, O. Farkas, J. B. Foresman, J. V. Ortiz, J. Cioslowski, D. J. Fox, Gaussian Inc., Wallingford CT, **2009**.
[48] M. Peña-Alvarez, P. M. Burrezo, M. Kertesz, T. Iwamoto, S. Yamago, J. Xia, R. Jasti, L. J. T. Navarrete, M. Taravillo, V. G. Baonza, J. Casado, *Angew. Chem. Int. Ed*. **2014**, *53*, 7033.

[49] J.-L. Bredas, R. R. Chance, R. Silbey, *Phys. Rev. B* **1982**, *26*, 5843.
[50] L. Cuff, C. X. Cui, M. Kertesz, *J. Am. Chem. Soc*. **1994**, *116*, 9269.
[51] G. Lucazeau, *J. Raman Spectrosc.* **2003**, *34*, 478.
[52] R. W. Munn, *Phys. Rev. B* **1975,** *12,* 3491.
[53] J. J. Flores, E. L. Chronister, *J. Raman spectr.* **1996**, *27*, 149.
[54] L. Qiu, M. Peña-Alvarez, M. Taravillo, P.J. Evans, E.R. Darzi, R. Jasti, P.M.L. Burrezo, J.T. Navarrete, V.G. Baonza, J. Casado, M. Kertesz, *Chem. Eur. J.* **2017**, *23*,16593.